POLYOXOMETALATES

Open Access
RESEARCH ARTICLE

Silverton-type polyoxometalate-derived electrocatalyst for efficient hydrogen evolution in acidic and alkaline media

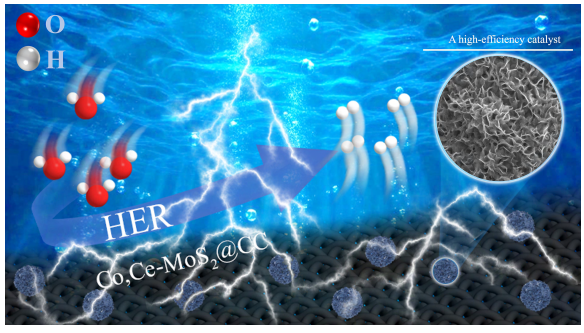
Pingfan Wu[1,2] ✉, Xiao Feng[1], Sizhan Shu[1], Shuxin Zhang[1], Yuhan Li[1], Yujiao Huang[1], Shengyang Ou[1], Jun Sun[1], and Qiaoshun Chen[1]

[1] *Hubei University of Technology, Institute of Polyoxometalate-Based Materials, Hubei Provincial Key Laboratory of Green Materials for Light Industry, New Materials and Green Manufacturing Talent Introduction and Innovation Demonstration Base, Wuhan 430068, China*
[2] *Hubei Longzhong Lab, Xiangyang 441000, China*

Cite This: *Polyoxometalates*, **2026**, *5*, 9140156

Read Online

ABSTRACT: Highly efficient and durable nonnoble-metal electrocatalysts for the hydrogen evolution reaction (HER) are essential for large-scale green hydrogen production. In this work, a trimetallic polyoxometalate precursor, $H_2[Co(NH_3)_6]_2[CeMo_{12}O_{42}]$, was synthesized via polyoxometalate self-assembly. Subsequently, a Co,Ce-codoped MoS_2 electrocatalyst (Co,Ce-MoS_2@CC) was grown *in situ* on carbon cloth (CC) through one-step hydrothermal sulfidation. This precursor strategy effectively avoids phase separation and interfacial mismatch—the two major drawbacks of conventional doping routes. Experimental results combined with density functional theory calculations revealed that Ce^{3+}/Ce^{4+} redox pairs modulate the interfacial charge distribution in the catalyst. Doped Co species serve as electron acceptors to counterbalance the electron enrichment induced by Ce, optimizing HER kinetics and the adsorption/desorption free energies of reaction intermediates. In 1.0 M KOH, the optimized Co,Ce-MoS_2@CC requires an overpotential of only 58 mV to deliver 10 mA·cm⁻, and 118 mV in 0.5 M H_2SO_4. It maintains stable performance over 72 h at a current density of 100 mA·cm^{-2} in both alkaline and acidic electrolytes. This work proposes a polyoxometalate precursor-mediated Co,Ce-codoping strategy, offering a promising route for the scalable fabrication of high-performance, nonnoble-metal MoS_2 electrocatalysts for the HER.



KEYWORDS: hydrogen evolution reaction (HER), atomic doping, polyoxometalates, MoS_2, electrocatalysis, density functional theory (DFT)

1 Introduction

Low-cost, high-performance nonnoble-metal catalysts are essential alternatives to noble-metal catalysts for scalable hydrogen production via water electrolysis [1–4]. Among transition-metal dichalcogenides, molybdenum disulfide (MoS_2) has emerged as a promising nonnoble-metal electrocatalyst owing to the high intrinsic activity of its edge sites, robust structure, and natural abundance [5–7]. Thus, extensive research has focused on engineering MoS_2 as a viable alternative to noble-metal catalysts for the hydrogen evolution reaction (HER) [8]. However, owing to the semiconducting nature of the 2H phase and the inertness of its basal plane, the overall catalytic performance of MoS_2 still lags behind that of state-of-the-art noble-metal electrocatalysts [9, 10].

To activate the inert basal plane of MoS_2, a series of modification strategies have been proposed, including elemental doping, heterostructure fabrication, and defect engineering [11–14]. Among these, transition-metal doping effectively modulates the electronic band structure, promotes charge transport, and reconstructs the basal-plane electronic states, thereby activating inert sites [15–17]. For instance, Co-doped MoS_2 and Cu single atom-doped MoS_2 exhibit substantially higher HER activity than pristine MoS_2 [18, 19]. In another study, density functional theory (DFT) calculations revealed hydrogen adsorption free energies (ΔG_H^*) of −0.33 eV for Co@MoS_2 and −0.75 eV for Ni@MoS_2, indicating that doping thermodynamically favors hydrogen adsorption [20]. However, the catalytic activity of these singly doped systems is still substantially lower than that of Pt (ΔG_H^* = 0.09 eV) [21, 22].

Rare-earth elements (e.g., Ce, La, and Nd) possess unique 4f electron configurations, variable oxidation states, and reversible charge-transfer characteristics, offering distinct advantages for electronic-structure modulation [23, 24]. Particularly, the reversible Ce^{3+}/Ce^{4+} redox pair can act as a charge-buffering center to dynamically regulate the local charge density at active sites [25, 26]. Zhao et al. revealed that this electron-buffering effect enables the reversible tuning of electron density at metal centers [27]. Additionally, Li et al. verified the efficacy of rare-earth elements in

Received: June 13, 2026; **Revised:** August 7, 2026
Accepted: August 24, 2026

✉Address correspondence to pingfanwu-111@163.com

https://doi.org/10.26599/POM.2026.9140156

charge regulation for electrocatalyst engineering [28]. However, Ce-doping of MoS_2 can cause excessive electron accumulation at active sites, resulting in overly strong adsorption of hydrogen intermediates and thus limiting catalytic performance [29]. To address this issue, a transition metal with moderate electron-withdrawing ability (e.g., Co) can be introduced as a secondary dopant. Through charge delocalization, the Co dopant relieves the Ce-induced excess electron density on adjacent S active sites, thereby optimizing ΔG_{H^*} [30, 31]. Recently, Jiang et al. fabricated a $CeO_2/Co_4N@Ni_3S_2$ flower-like heterostructure on nickel foam, utilizing dual active sites to facilitate low-barrier water activation and rapid hydrogen desorption [32]. Similarly, Li et al. constructed carbon nanotube-bridged CeO_2–CoP hierarchical hollow nanocubes, leveraging abundant metal heterointerfaces to promote interfacial electron transfer and regulate intermediate adsorption [33].

A prerequisite for fully exploiting this Co–Ce synergy is the fabrication of highly uniform, strongly coupled catalysts. At the same time, conventional doping strategies (e.g., chemical vapor deposition, multistep hydrothermal synthesis, and physical mixing) often lead to inhomogeneous dopant distributions, impurity-phase formation, and interfacial lattice mismatch, which hinder charge transport, reduce structural stability, and constrain catalytic performance [34, 35]. In contrast, integrating multiple metals into a single molecular precursor effectively improves catalyst uniformity [36–38]. Among various platforms, polyoxometalates (POMs) combine structural tunability and chemical multifunctionality, making them ideal precursors for constructing multimetallic assemblies [39–41]. POMs are discrete anionic metal-oxide clusters composed of early transition metals (e.g., Mo, W, V, Nb, and Ta) linked by oxygen bridges via corner- or edge-sharing polyhedra [39]. They feature rigid frameworks, high thermal stability, and rich redox chemistry, with electronic structures that can be tuned through heteroatom incorporation [42, 43]. Moreover, their abundant negatively charged surface sites allow the effective anchoring of cationic species, providing compositional flexibility for constructing multimetallic systems [44, 45]. For example, $(NH_4)_6H_2[CeMo_{12}O_{42}]$ ($CeMo_{12}$) is a Silverton-type derivative in which 12 molybdenum–oxygen octahedra surround a central Ce atom, integrating Ce and Mo at the molecular level while endowing the cluster with a high negative charge [46]. Into this system, Co can be introduced as complex cations, such as $[Co(NH_3)_6]^{3+}$, which form a stable ion-pair complex with the anionic POM cluster through Coulombic attraction. At the same time, the NH_3 ligands act as hydrogen-bond donors, creating a hydrogen-bond network with the surface oxygen atoms of $CeMo_{12}$. This further enhances the structural and thermal stability of the precursor [47, 48]. Owing to the structural homogeneity of POM precursors, high-temperature sulfidation effectively suppresses metal segregation and yields well-dispersed multimetallic sulfides with dense and uniformly distributed active sites [49–51].

Based on the above considerations, the Silverton-type POM $CeMo_{12}$ was selected as the molecular precursor to synthesize $H_2[Co(NH_3)_6]_2[CeMo_{12}O_{42}]$ (Co_2CeMo_{12}) via cation exchange with $[Co(NH_3)_6]^{3+}$. Through one-step hydrothermal sulfidation and calcination, a Co,Ce-codoped MoS_2 electrocatalyst (Co,Ce-MoS_2@CC) was constructed *in situ* on carbon cloth (CC). Additionally, Co-MoS_2@CC, Ce-MoS_2@CC, and MoS_2@CC were prepared as control samples to elucidate the effects of different metal combinations on the material architecture, electronic properties, and catalytic performance. Additionally, a Co,Ce-MoS_2@CC-MS control sample was prepared from discrete metal salts (rather than POM precursors) to validate the effectiveness of the employed precursor strategy. This work aimed to harness the synergy between rare-earth and transition-metal dopants in MoS_2 to develop high-performance, durable nonnoble-metal HER electrocatalysts, offering a viable material platform and experimental insights for the practical deployment of hydrogen technologies.

2 Methods and materials

The details on the synthesis of certain raw materials, characterization methods, and electrochemical tests are provided in the Electronic Supplementary Material (ESM).

2.1 Synthesis of Co_2CeMo_{12}

To prepare Solution 1, 2.50 mmol of $CeMo_{12}$ was combined with 100 mL of 0.1 M H_2SO_4, followed by stirring for 1 h at ambient temperature, yielding a pale-yellow translucent liquid. In a separate vessel, 7.48 mmol of $[Co(NH_3)_6]Cl_3$ was dissolved in 25 mL of deionized water, producing an orange-red solution (Solution 2). Solution 2 was added dropwise to Solution 1 under constant agitation, forming a beige solid. This precipitate was filtered out, washed three times with ethanol, and air-dried prior to further use.

2.2 Catalyst synthesis

Synthesis of Co,Ce-MoS_2@CC: First, 0.30 mmol of Co_2CeMo_{12} and 18.80 mmol of thiourea were dispersed in 30 mL of deionized water under stirring for 1 h at ambient temperature. A piece of CC (dimensions: 3 cm × 2 cm) was immersed in the resulting solution. The entire system was then transferred into a 50 mL Teflon-lined autoclave and maintained at 180 °C for 24 h. After natural cooling, the modified CC was retrieved, sequentially washed with deionized water and absolute ethanol, and dried under vacuum at 60 °C for 12 h. The dry sample was loaded into a tube furnace and annealed under a continuous flow of 5% H_2 in Ar. The furnace temperature was increased stepwise to 300, 400, and 500 °C at a ramp rate of 5 °C·min^{-1}, with a dwelling time for 2 h at each target temperature. The resulting products were denoted as Co,Ce-MoS_2@CC-300, Co,Ce-MoS_2@CC (calcined at 400 °C), and Co,Ce-MoS_2@CC-500, respectively.

Synthesis of Ce-MoS_2@CC: Ce-MoS_2@CC was synthesized using the same procedure as for Co,Ce-MoS_2@CC, but with Co_2CeMo_{12} replaced by $CeMo_{12}$ and calcination performed at 400 °C.

Synthesis of Co-MoS_2@CC: Co-MoS_2@CC was synthesized using the same procedure as for Co,Ce-MoS_2@CC, but with Co_2CeMo_{12} replaced by $(NH_4)_6[Co_2Mo_{10}O_{38}H_4]\cdot 11H_2O$ (Co_2Mo_{10}) and calcination performed at 400 °C.

Synthesis of MoS_2@CC: MoS_2@CC was synthesized using the same procedure as for Co,Ce-MoS_2@CC, but with Co_2CeMo_{12} replaced by $(NH_4)_6Mo_7O_{24}$ and calcination performed at 400 °C.

Synthesis of Co,Ce-MoS_2@CC-MS: Co,Ce-MoS_2@CC-MS was synthesized using the same procedure as for Co,Ce-MoS_2@CC, but with Co_2CeMo_{12} replaced by equivalent molar amounts of conventional metal salts ($CoCl_2\cdot 6H_2O$, $(NH_4)_2Ce(NO_3)_6$, and $(NH_4)_6Mo_7O_{24}\cdot 4H_2O$) with the same Co:Ce:Mo molar ratio (2:1:12) and calcination performed at 400 °C.

Synthesis of Pt/C@CC: A commercial Pt/C catalyst (20 wt.% Pt) was dispersed in a Nafion-isopropanol mixture, followed by ultrasonication for 20 min, producing a homogeneous suspension.

A 1 cm × 1 cm region on an activated CC strip (1 cm × 2 cm) was defined using a mask for subsequent catalyst deposition. The suspension was drop-cast onto this exposed area. After resting for 10 min at room temperature, the substrate was vacuum-dried at 60 °C overnight, yielding the Pt/C@CC electrode.

2.3 Computational details

All first-principles DFT computations were performed using the CASTEP and DMol3 modules in Materials Studio [52]. Detailed computational parameters are provided in the ESM.

3 Results and discussion

3.1 Synthesis and structural characterization

Figure 1(a) schematically presents the fabrication of the Co,Ce-MoS_2@CC nanocomposite, where Co,Ce-codoped MoS_2 nanosheet arrays were *in situ* grown on the CC surface from Co_2CeMo_{12}, thiourea, and CC via one-step hydrothermal sulfidation followed by calcination.

Figure 1(b) compares the infrared spectra of Co_2CeMo_{12}, $CeMo_{12}$, and $[Co(NH_3)_6]Cl_3$. After cation exchange, the characteristic peak of NH_4^+ at 1,403 cm^{-1} disappeared, but two new peaks appeared at 1,328 cm^{-1} (N–H symmetric bending vibration) and 827 cm^{-1} (N–H rocking vibration), indicating that $[Co(NH_3)_6]^{3+}$ successfully replaced NH_4^+ [53]. More importantly, the key skeletal vibrations of the $[CeMo_{12}O_{42}]^{8-}$ anion are fully retained in the spectrum of Co_2CeMo_{12}: the peaks near 950 and 900 cm^{-1} were ascribed to terminal Mo=O stretching, and broad features in the 500–900 cm^{-1} region were assigned to Ce–O vibrations [46]. The persistence of these representative signals in the fingerprint region confirms that cation exchange did not disrupt the core POM skeleton.

Figure 1(c) presents the powder X-ray diffraction (PXRD) patterns of Co,Ce-MoS_2@CC and MoS_2@CC. Both samples exhibit diffraction peaks at 2θ of 14.1°, 32.8°, 40.3°, and 58.9°, corresponding to the (002), (101), (103), and (110) planes of MoS_2 (PDF#37-1492). No characteristic signals of Co or Ce sulfides were detected over the entire scanning range, indicating that the introduced Co and Ce neither formed new crystalline phases nor disrupted the intrinsic structure of MoS_2.

X-ray photoelectron spectroscopy (XPS) was utilized to

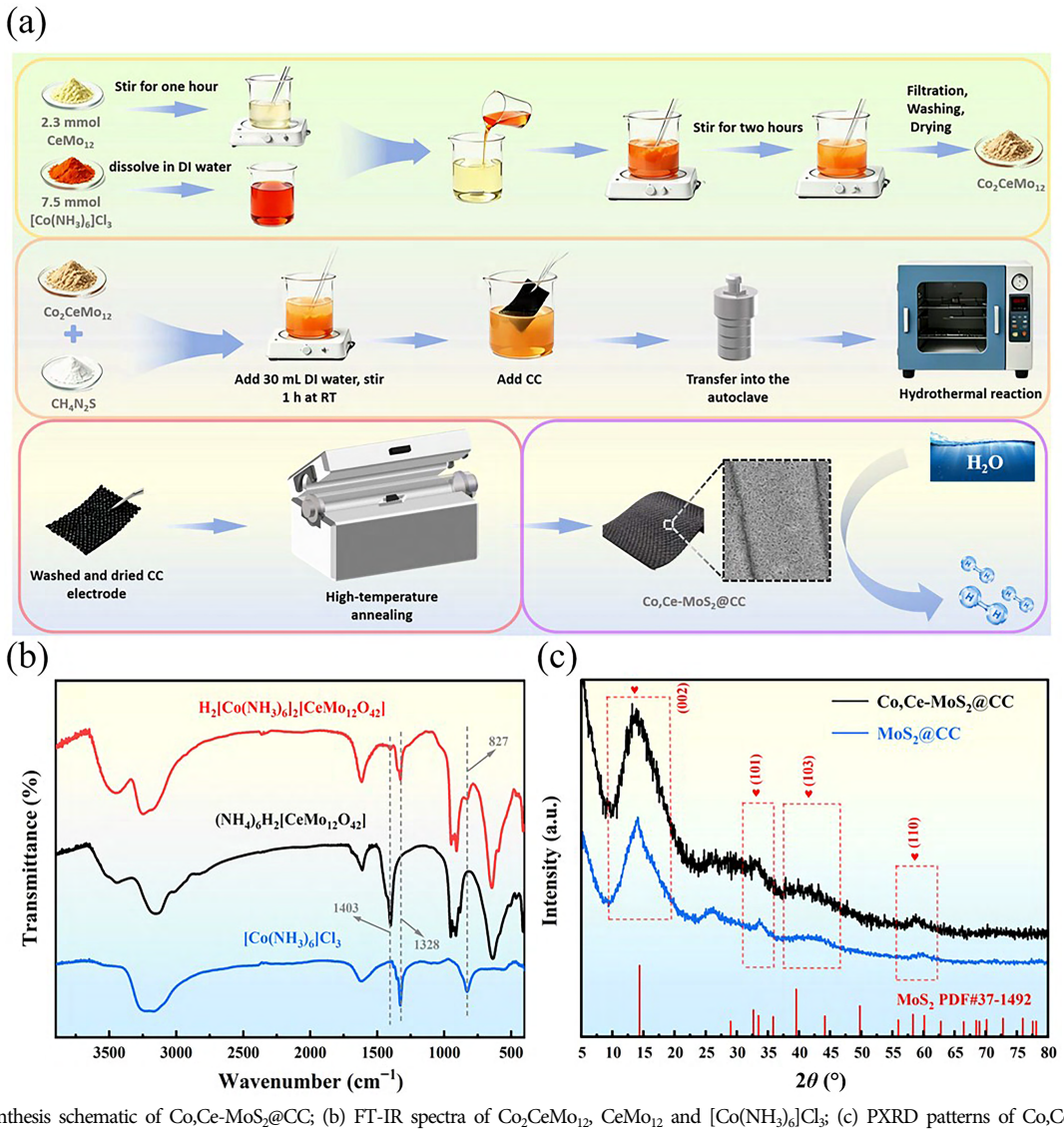


Figure 1 (a) Synthesis schematic of Co,Ce-MoS_2@CC; (b) FT-IR spectra of Co_2CeMo_{12}, $CeMo_{12}$ and $[Co(NH_3)_6]Cl_3$; (c) PXRD patterns of Co,Ce-MoS_2@CC and MoS_2@CC.

characterize the valence states and chemical environments of the elements in Co,Ce-MoS_2@CC (Fig. 2). The survey spectrum (Fig. S1 in the Electronic Supplementary Material (ESM)) features the signals of six elements: Co, Ce, Mo, S, O, and C. In the high-resolution Co 2p spectrum (Fig. 2(c)), the peaks at 783.8 eV ($2p_{3/2}$) and 800.3 eV ($2p_{1/2}$) were assigned to Co^{2+}, whereas those at 779.8 and 795.1 eV correspond to Co^{3+} [33]. Satellite signals near 787.5 and 805.0 eV corroborate the coexistence of both oxidation states, indicating that Co adopts a mixed-valence configuration within the MoS_2 lattice [50]. In the Ce 3d spectrum (Fig. 2(d)), the characteristic multiplet splitting reflects the presence of Ce^{3+} and Ce^{4+}: Peaks at 887.6 and 905.9 eV were attributed to Ce^{4+}, whereas those at 884.1 and 902.1 eV arise from Ce^{3+}, confirming a mixed +3/+4 valence state [29]. In the Mo 3d spectrum (Fig. 2(b)), the dominant doublet at 230.0 eV ($3d_{5/2}$) and 233.0 eV ($3d_{3/2}$) corresponds to Mo^{4+} in the MoS_2 phase [5]. A shoulder at 227.1 eV originates from the S 2s core level of Mo–S bonds, further confirming the formation of the MoS_2 framework. Weak signals centered at 232.9 and 236.0 eV indicate a minor MoO_3 component, likely arising from surface oxidation during sample preparation or hydrothermal treatment [53]. In the S 2p spectrum (Fig. 2(a)), two prominent peaks at 162.8 and 164.0 eV correspond to the S $2p_{3/2}$

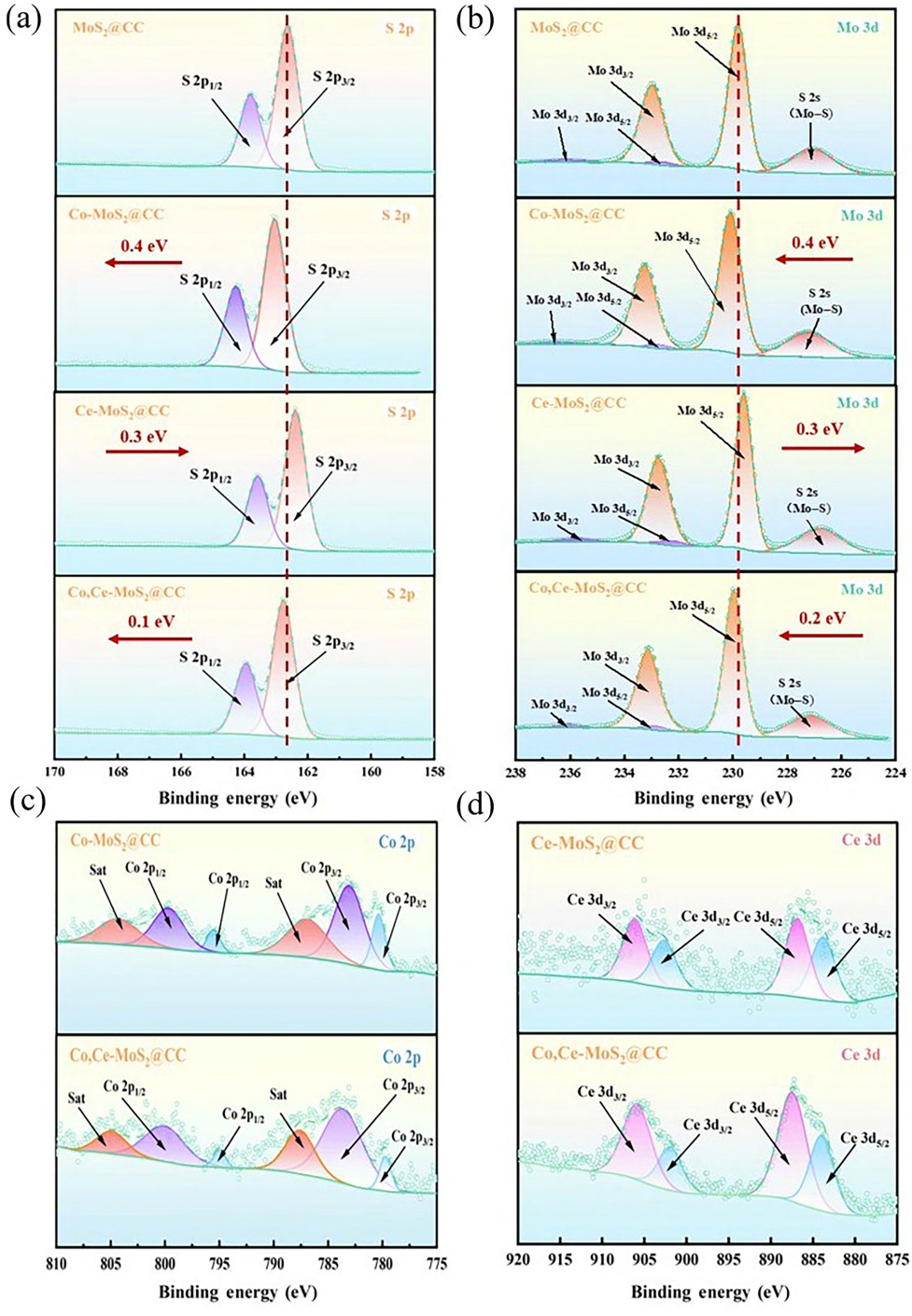


Figure 2 XPS spectra of (a) S 2p, (b) Mo 3d, (c) Co 2p, and (d) Ce 3d of the MoS_2@CC, Ce-MoS_2@CC, Co-MoS_2@CC and Co,Ce-MoS_2@CC.

and S $2p_{1/2}$ spin-orbit doublets of S^{2-} bonded to Mo, aligning with the MoS_2 structure [6]. Comparison with undoped MoS_2@CC reveals notable binding-energy shifts that provide valuable insight into the electronic interactions induced by heteroatom incorporation. Specifically, the Mo 3d and S 2p core levels in Ce-MoS_2@CC are downshifted by 0.3–0.4 eV, consistent with electron donation from Ce into the MoS_2 host and an increased charge density around both Mo and S centers. In stark contrast, singly doped Co-MoS_2@CC exhibits a positive shift of 0.4 eV for the same core levels, indicating that Co withdraws charge from the Mo–S framework, reducing electron density at these sites [53]. Interestingly, the codoped Co,Ce-MoS_2@CC registers only a slight positive shift of 0.1–0.2 eV, intermediate between the values for the individual dopants. This behavior suggests that the electron-donating effect of Ce partially counterbalances the electron-withdrawing nature of Co, establishing a well-balanced charge distribution [12, 54].

These shifts reveal internal electron redistribution: Ce injects a small quantity of electrons into the MoS_2 matrix, increasing the electron density at Mo and S and thus lowering their binding energies. In contrast, Co acts as an electron acceptor, withdrawing electrons from the Mo–S network, reducing the electron density at Mo and S, and raising their binding energies [55–57]. The opposite electron-transfer directions induced by Co and Ce establish a built-in electric field across the MoS_2 host lattice, as evidenced by the opposite binding energy shifts [58, 59]. This local field effect facilitates the spatial separation of charges and optimizes the adsorption/desorption of intermediates during HER [60, 61].

Figure 3 presents the morphological and microstructural features of Co,Ce-MoS_2@CC. Scanning electron microscopy (SEM) images (Fig. 3(a)) reveal a "nanowrinkled" surface morphology formed via the stacking of layered structures; these wrinkles interweave, forming a three-dimensional porous structure with an undulating topography. This structure increases the electrochemically active surface area (ECSA) and exposes the active edge sites of MoS_2, thereby enhancing catalytic performance [62].

Transmission electron microscopy (TEM) images (Figs. 3(b)–3(d)) further reveal the microstructure of the catalyst. The sample retains the typical two-dimensional layered assembly characteristics of MoS_2, exhibiting a "nanoflower" structure formed via nanosheet aggregation. High-resolution TEM (HRTEM) images (Fig. 3(c)) show multiple lattice fringes assigned to the (002), (101), (103), and (006) planes of MoS_2, consistent with the PXRD results. Notably, local discontinuities or distortions are observed in some intralayer lattice fringes, indicating abundant structural defects in the MoS_2 matrix, which can serve as active centers for catalytic reactions [63].

Elemental maps (Fig. 3(e)) confirm that MoS_2 constitutes the continuous matrix, with uniformly dispersed Ce and Co. Quantitative inductively coupled plasma mass spectrometry (ICP-MS) (Table S1 in the ESM) further confirms the incorporation of Co and Ce, yielding Co/Ce and Mo/Ce molar ratios of approximately 2.1 and 7.1, respectively.

3.2 HER performance in an alkaline medium

HER performance of the catalysts was evaluated in an alkaline medium (Fig. S2 in the ESM). The results reveal that Co,Ce-MoS_2@CC calcined at 400 °C exhibits the best catalytic activity; thus, this electrode was employed in all subsequent electrochemical tests. Specifically, in 1.0 M KOH, Co,Ce-MoS_2@CC requires an overpotential of only 58 mV to achieve 10 mA·cm^{-2}, lower than those of Co-MoS_2@CC (115 mV), Ce-MoS_2@CC (154 mV), MoS_2@CC (198 mV), and CC (588 mV; Fig. 4(a)). This indicates that the synergistic Co,Ce-codoping strategy effectively boosts the electrocatalytic HER performance of MoS_2 [60].

Tafel slope analysis (Fig. 4(d)) provided further insight into the HER reaction kinetics [63]. The HER typically proceeds via the Volmer, Heyrovsky, and Tafel steps, with corresponding theoretical Tafel slopes of 120, 40, and 30 mV·dec^{-1} [64]. A Tafel slope of 51.54 mV·dec^{-1} was obtained for Co,Ce-MoS_2@CC, substantially smaller than those for Ce-MoS_2CC (96.31 mV·dec^{-1}), Co-MoS_2@CC (101.97 mV·dec^{-1}), MoS_2@CC (108.29 mV·dec^{-1}), and CC (116.21 mV·dec^{-1}). These results indicate faster reaction kinetics over Co,Ce-MoS_2@CC, consistent with its HER performance [65].

Interfacial charge transfer kinetics were characterized using electrochemical impedance spectroscopy. The experimental data were fitted using the Randles equivalent circuit model, which includes solution resistance (R_s), charge-transfer resistance (R_{ct}), and a constant phase element [66]. From the Nyquist plots (Fig. 4(e) and Table S5 in the ESM), the R_{ct} values increase in the order of Co,Ce-MoS_2@CC (2.49 Ω) < Co-MoS_2@CC (6.28 Ω) < Ce-MoS_2@CC (26.45 Ω) < MoS_2@CC (120.60 Ω) < CC (257.20 Ω). These results confirm that Co and Ce effectively accelerate interfacial electron transfer and enhance electrical conductivity [67].

Cyclic voltammetry (CV) was performed for all catalysts within the potential window where Faradaic processes do not occur [12]. ECSA (Table S3 in the ESM) was determined from the measured double-layer capacitance (C_{dl}, Fig. 4(f)) [13]. Co,Ce-MoS_2@CC exhibits the highest C_{dl} (144.06 mF·cm^{-2}), substantially surpassing Ce-MoS_2@CC (91.76 mF·cm^{-2}), Co-MoS_2@CC (70.34 mF·cm^{-2}), MoS_2@CC (47.70 mF·cm^{-2}), and CC (2.95 mF·cm^{-2}). This indicates that codoping yields the largest active surface area, exposing abundant active sites to promote the HER [65]. To evaluate intrinsic catalytic activity, geometric current densities at an overpotential of 150 mV in an alkaline medium were extracted from the linear sweep voltammetry polarization curves and normalized by the corresponding ECSA values (Table S3 in the ESM) [68]. Additionally, mass activities were calculated at the same overpotential based on the catalyst mass loadings (Table S2 in the ESM). The resulting comparisons are summarized in Fig. S8 in the ESM, where Co,Ce-MoS_2@CC exhibits the highest ECSA-normalized current density and mass activity, confirming its superior intrinsic catalytic activity [69, 70].

The reaction mechanism was further elucidated using DFT calculations. Figure 4(g) presents the Gibbs free energy diagram for the alkaline HER pathway on Co,Ce-MoS_2@CC. The results reveal a water dissociation energy barrier of 1.30 eV for this codoped structure, providing theoretical insight into the HER pathway over this Co,Ce-codoped configuration in alkaline media.

3.3 HER performance in an acidic medium

Next, the HER activity of the Co,Ce-MoS_2@CC series was measured in 0.5 M H_2SO_4 (Fig. S3 in the ESM). The sample annealed at 400 °C required an overpotential of only 118 mV to deliver 10 mA·cm^{-2}—substantially lower than the 178 mV for Co-MoS_2@CC, 151 mV for Ce-MoS_2@CC, 218 mV for MoS_2@CC, and 446 mV for CC. Its Tafel slope (58.98 mV·dec^{-1}) is also superior to those of Co-MoS_2@CC (96.53 mV·dec^{-1}), Ce-MoS_2@CC (84.39 mV·dec^{-1}), MoS_2@CC (117.58 mV·dec^{-1}), and CC (124.97 mV·dec^{-1}) (Fig. 5(d)). This confirms the faster reaction kinetics over

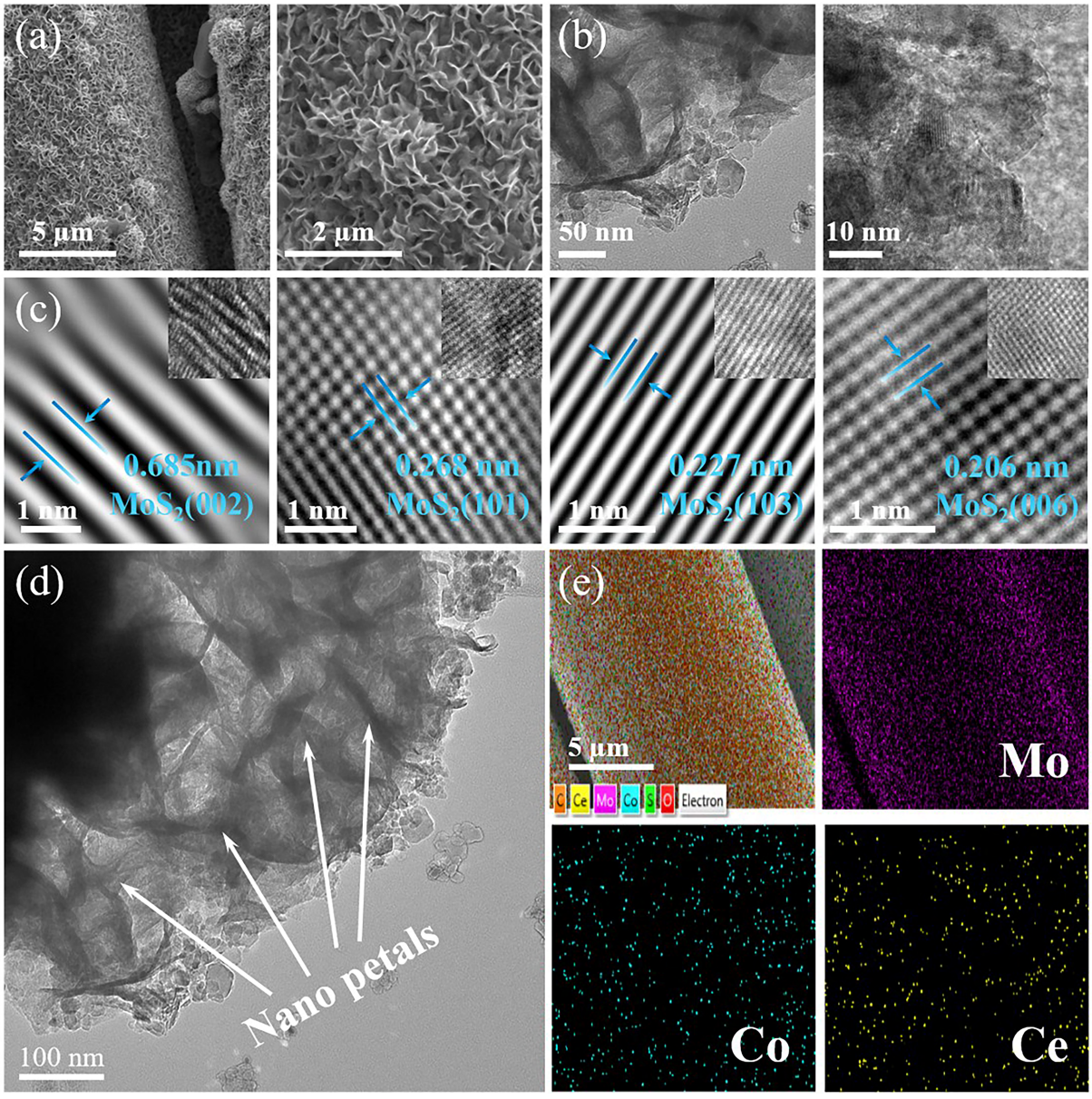


Figure 3 (a) SEM images of Co,Ce-MoS_2@CC at different magnifications; (b)–(d) TEM and HRTEM images of Co,Ce-MoS_2@CC; (e) elemental mapping.

Co,Ce-MoS_2@CC in an acidic medium.

The C_{dl} value for Co,Ce-MoS_2@CC (103.14 mF·cm^{-2}), determined from CV data (Fig. S6 in the ESM), greatly exceeds the values for the reference samples. This provides additional evidence for the greater ECSA and higher density of accessible active sites in the codoped catalyst. We further calculated the ECSA-normalized current densities and mass activities (Fig. S8 in the ESM) based on ECSA (Table S4 in the ESM) and mass loadings (Table S2 in the ESM), respectively, with the results further confirming the superior intrinsic catalytic activity of Co,Ce-MoS_2@CC.

Electrochemical impedance spectroscopy reveals that Co,Ce-MoS_2@CC has the smallest charge transfer resistance (R_{ct} = 10.47 Ω) among all samples (Table S5 in the ESM), outperforming Co-MoS_2@CC (32.65 Ω), Ce-MoS_2@CC (47.39 Ω), MoS_2@CC (114.80 Ω), and CC (305.70 Ω). These findings confirm its excellent interfacial electron transfer ability.

The reaction mechanism in acidic media was further elucidated using DFT calculations (Fig. 5(g)). The calculated hydrogen adsorption free energy (ΔG_H^*) for the Co,Ce-codoped structure is −0.28 eV, which is closer to zero compared to that for the pristine 2H-MoS_2 basal plane (1.67 eV), indicating that codoping optimizes the hydrogen intermediate adsorption strength and facilitates acidic HER.

The above findings indicate that Co,Ce-MoS_2@CC exhibits the highest HER activity in both alkaline and acidic environments among the considered samples. This was attributed to the synergistic effects of Co,Ce-codoping: it not only optimizes the electronic structure of MoS_2, increasing the number of active sites, but also facilitates interfacial charge transfer and reduces R_{ct}, thereby substantially enhancing the overall electrochemical activity of the catalyst and accelerating reaction kinetics [71].

To further validate the advantages of the POM-precursor route employed herein, we systematically compared the electrochemical performance of the POM-derived sample with that of a control synthesized from discrete metal salts (Co,Ce-MoS_2@CC-MS; Figs. S4 and S5 in the ESM). The observed performance enhancement is

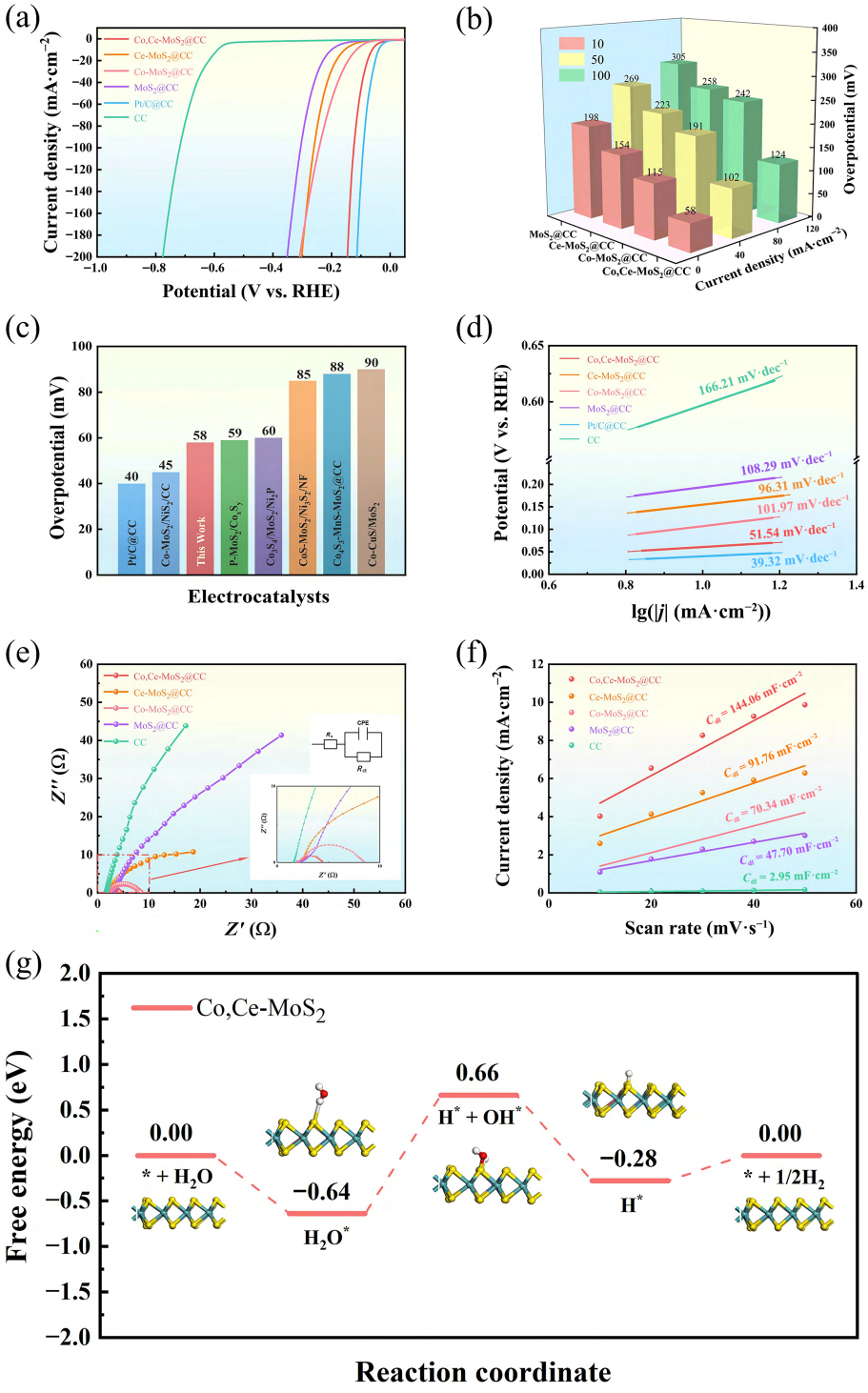


Figure 4 HER performance of the catalysts in 1 M KOH: (a) LSV curves; (b) overpotentials; (c) η_{10} histogram comparing Co,Ce-MoS_2@CC with reported MoS_2-based catalysts; (d) Tafel slopes; (e) Nyquist plots; (f) C_{dl} curves; (g) Gibbs free energy diagrams for the alkaline HER pathway.

consistent with the expected benefits of the POM-precursor route [72, 73].

3.4 Stability and durability

To assess the practical viability of the catalyst, the cyclic stability and long-term durability of Co,Ce-MoS_2@CC were systematically investigated. To evaluate cyclic stability, linear sweep voltammetry profiles recorded before and after 5,000 CV cycles were compared (Figs. 6(a) and 6(c)). At a current density of 100 mA·cm^{-2} in alkaline and acidic media, the overpotential increases by merely 2 and 4 mV, respectively, indicating good cycling stability.

Long-term durability was further evaluated via *i*–*t* tests. Chronoamperic measurements were conducted for 72 h in 1.0 M KOH and 0.5 M H_2SO_4 at a constant current density (100 mA·cm^{-2}) [12], showing no notable performance degradation for Co,Ce-MoS_2@CC (Figs. 6(b) and 6(d)).

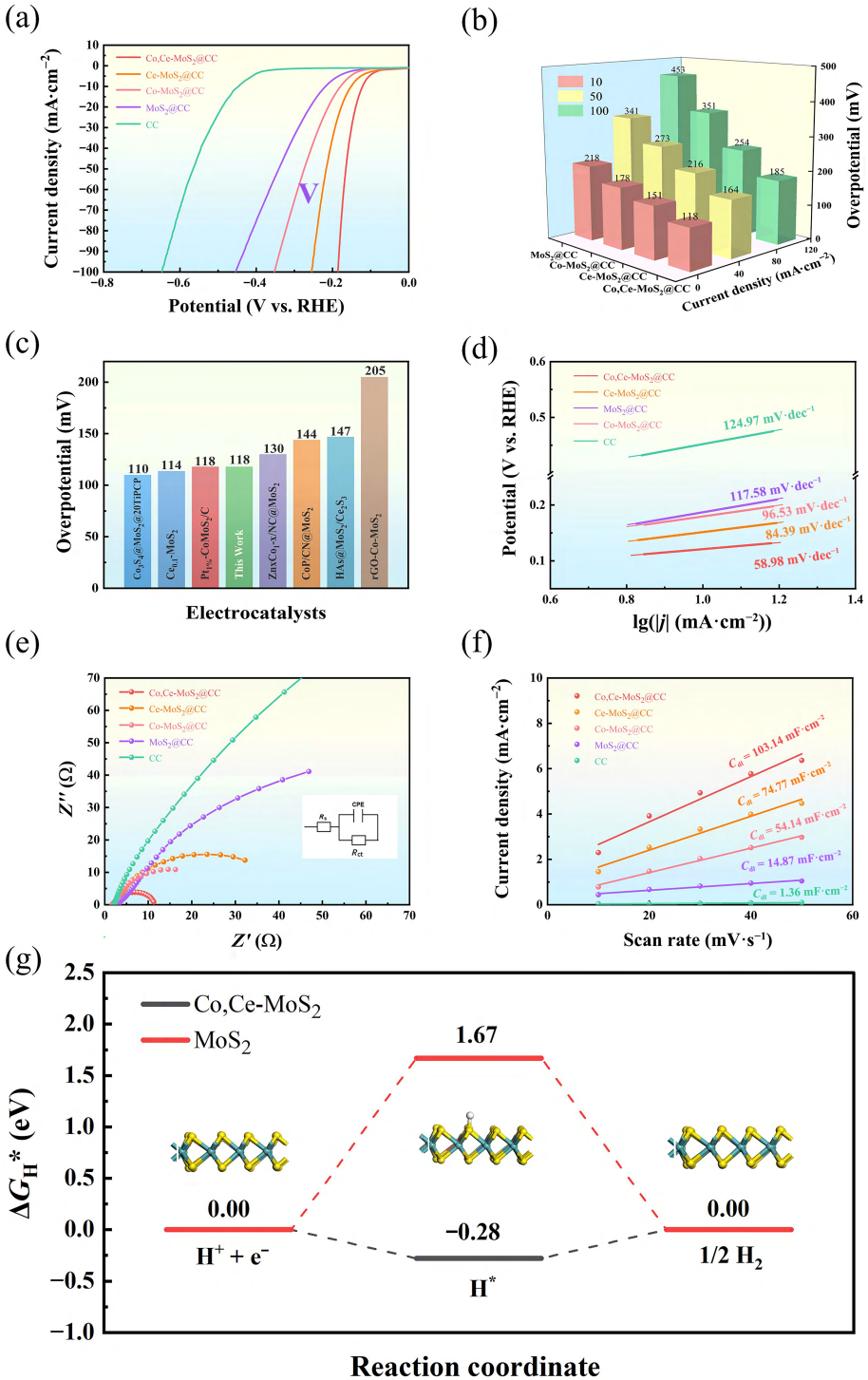


Figure 5 Electrochemical performance of catalysts in 0.5 M H_2SO_4: (a) LSV curves; (b) overpotentials; (c) η_{10} comparison with reported MoS_2-based catalysts; (d) Tafel slopes; (e) Nyquist plots; (f) C_{dl} curves; (g) Gibbs free energy diagrams for the acidic HER pathway.

After stability testing, the samples were characterized using scanning electron microscopy to investigate their structural stability (Fig. S9 in the ESM) [71]. The original nanoflower and two-dimensional layered structures of the catalyst remained intact after the tests, without notable deformation, collapse, or damage. Furthermore, the PXRD pattern of the poststability-test electrode (Fig. S10 in the ESM) reveals no additional diffraction peaks of impurity phases, confirming the preservation of the primary MoS_2 crystalline structure. However, peak intensity slightly decreases, likely because of partial surface amorphization or minor material loss during prolonged cycling [74]. Additionally, high-resolution Ce 3d XPS spectra of the catalyst recorded after 72 h of durability testing (Figs. S11 and S12 in the ESM) show that the peak positions and area ratios of Ce^{3+} and Ce^{4+} remain essentially unchanged relative to the pristine sample, indicating that the mixed-valence state (+3/+4) of Ce is well-preserved during long-term electrochemical cycling. Collectively, these characterizations confirm that Co,Ce-MoS_2@CC possesses robust structural, phase,

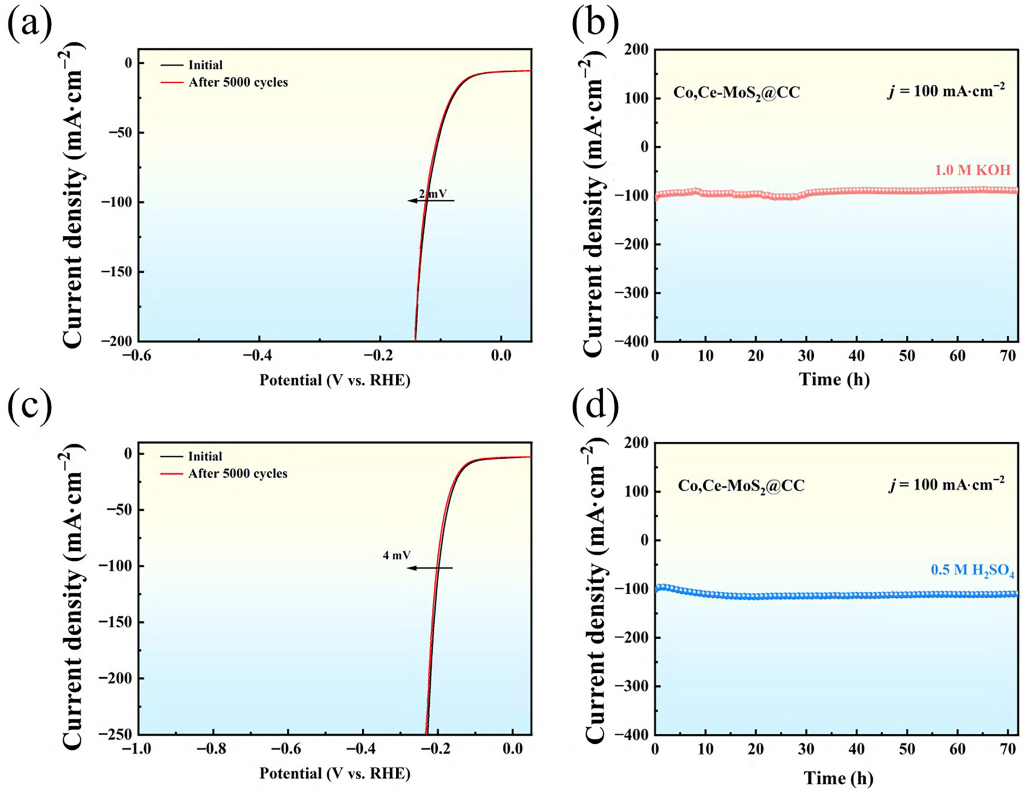


Figure 6 (a) and (b) LSV curves before/after 5000 CV cycles and 72 h *i*–*t* test (100 mA·cm^{-2}) of Co,Ce-MoS_2@CC in 1.0 M KOH; (c) and (d) in 0.5 M H_2SO_4.

and chemical stability, consistent with its good electrochemical durability [75].

3.5 Charge density difference analysis

The optimized atomic configuration after geometric relaxation (Fig. 7(a)) reveals that the substitution of Mo sites with Co and Ce atoms substantially reconstructs the local lattice configuration. The intrinsic Mo–S bond length is 2.427 Å, whereas the Co–S and Ce–S bond lengths are 2.310 and 2.789 Å, respectively. This asymmetric change in bond length induces in-plane microdistortions around the dopants and drives the anisotropic relaxation of the local lattice, forming the structural basis for subsequent electronic structure modulation.

Figure 7(b) presents the three-dimensional charge density difference map, showing the spatial polarization of charge distribution as isosurfaces. A pronounced charge depletion around the Ce atom (yellow isosurface) and a clear charge accumulation near the Co atom (blue isosurface) indicate a charge transfer pathway from Ce through S to Co [21, 76]. The plane-averaged charge density difference curve (along the *c*-direction) summarizes the vertical charge redistribution. Such nonuniform charge polarization is expected to induce local dipole moments and generate local electric fields, substantially affecting charge carrier separation and transport [77, 78].

To further resolve the in-plane charge distribution, a two-dimensional charge density difference slice on the Ce–Co–S coplanar layer was plotted (Fig. 7(c)). This slice shows decreased electron density at the Ce site and increased electron density at the Co site, thereby indicating the formation of a three-center charge redistribution network with Ce as the electron donor, Co as the electron acceptor, and S as the bridging mediator.

This synergistic mechanism explains the systematic binding energy shifts observed in XPS spectra and endows the material with excellent HER performance by optimizing charge transport [79].

4 Conclusions

This study reports a Co,Ce-MoS_2@CC catalyst derived from a single-source POM precursor. In alkaline and acidic media, the catalyst delivers a current density of 10 mA·cm^{-2} at overpotentials of 58 and 118 mV, respectively, and exhibits satisfactory long-term stability. This outstanding performance was attributed to several synergistic factors: (1) POM preassembly enables the uniform dispersion of Co, Ce, and Mo, whereas differences in ionic radii induce lattice distortion that activates the inert basal planes of MoS_2; (2) the Ce^{3+}/Ce^{4+} redox couple interacts with Co, establishing a donor–acceptor system, where directional charge transfer among Ce, S, and Co modulates the local electron density at active sites and enhances electron-transport efficiency; (3) *in situ* growth yields a three-dimensional hierarchical porous nanoarray, providing a high ECSA while establishing effective paths for electrolyte penetration and ion migration. Overall, this work provides fundamental insights into POM precursor-based codoping strategies for designing efficient nonnoble-metal HER electrocatalysts.

Electronic Supplementary Material: Supplementary material (electrochemical information, computational details, XPS, SEM, and other supporting data of catalysts) is available in the online version of this article at https://doi.org/10.26599/POM.2026.9140156.

Data availability

All data needed to support the conclusions in the paper are presented in the manuscript and the ESM. Additional data related

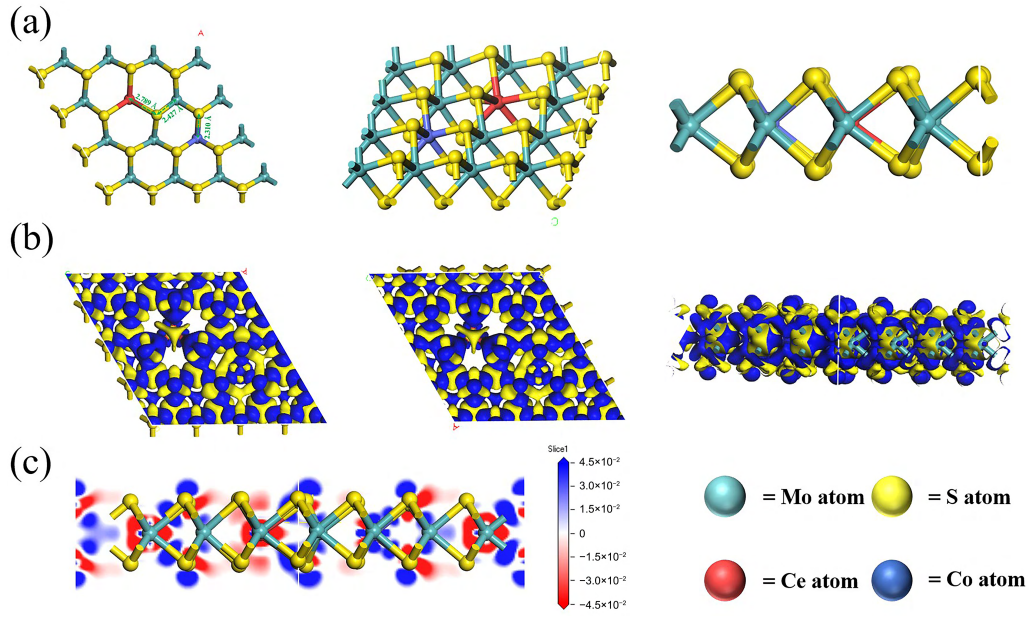


Figure 7 Theoretical computation results of Co/Ce co-doped monolayer MoS_2. (a) Optimized atomic structure. (b) 3D CDD plot showing charge redistribution (blue: accumulation, yellow: depletion). Inset: planar-averaged CDD curve along the *c*-direction. (c) 2D CDD slice along the Co-Ce-S coplanar layer (blue: accumulation, red: depletion).

to this paper may be requested from the corresponding author upon request.

Acknowledgements

The authors are grateful to the Institute of POM-based Materials, National College Students' Innovation and Entrepreneurship Training program (Nos. 202610500006 and 202610500005).

Declaration of competing interest

The authors declare that they have no known competing financial interests or personal relationships that could have appeared to influence the work reported in this paper.

Author contribution statement

P. F. W.: Conceptualization, project administration, funding acquisition, supervision, writing–review and editing. X. F.: Conceptualization, methodology, data curation, investigation, writing – original draft, writing – review & editing. S. Z. S.: Methodology, data curation, investigation, writing – review and editing. S. X. Z.: Methodology, data curation, investigation. Y. H. L.: Methodology, data curation, investigation. Y. J. H.: Methodology, data curation. S. Y. O.: Methodology, data curation. J. S.: Methodology, investigation. Q. S. C.: validation. All authors have approved the final manuscript.

Use of AI statement

None.

References

[1] Zhang, X. L.; Yu, P. C.; Sun, S. P.; Shi, L.; Yang, P. P.; Wu, Z. Z.; Chi, L. P.; Zheng, Y. R.; Gao, M. R. *In situ* ammonium formation mediates efficient hydrogen production from natural seawater splitting. *Nat. Commun.* **2024**, *15*, 9462.

[2] Li, J. Z.; Cheng, H. Y.; Sun, Y. N.; Ma, R. Z.; Li, D. N.; Xu, Y. C.; Jin, J. H.; Liu, X.; Shao, M. F.; Wang, L. Scalable ruthenium core-shell hydrogen catalyst for efficient and robust proton-exchange membrane electrolyser. *Nat. Mater.* **2026**, *25*, 238–248.

[3] Zhang, X. L.; Yu, P. C.; Su, X. Z.; Hu, S. J.; Shi, L.; Wang, Y. H.; Yang, P. P.; Gao, F. Y.; Wu, Z. Z.; Chi, L. P. et al. Efficient acidic hydrogen evolution in proton exchange membrane electrolyzers over a sulfur-doped marcasite-type electrocatalyst. *Sci. Adv.* **2023**, *9*, eadh2885.

[4] Xu, S. Y.; Wang, P.; Zhang, B. W.; Wang, C.; Low, J.; Ivanov, V. K.; Zhang, Z. M. Nickel-substituted polyoxometalate-CdS single-cluster photocatalysts for efficient plastic waste degradation coupled with H_2 production. *Polyoxometalates* **2025**, *4*, 9140096.

[5] Nadarajan, R.; Dey, S.; Kayal, A.; Mitra, J.; Shaijumon, M. M. Enhancing hydrogen evolution reaction activity through defects and strain engineering in monolayer MoS_2. *Chem. Sci.* **2024**, *15*, 18127–18134.

[6] Akir, S.; Schmiedecke, B.; Bagchi, D.; Plutnar, J.; Menezes, P. W.; Rodriguez-Ayllon, Y.; Lu, Y.; Sofer, Z.; Browne, M. P. 2D/2D heterojunction interfaces of 1T-MoS_2 and Ti_3C_2 MXene: Designing high-performance catalyst for the hydrogen evolution reaction. *npj 2D Mater. Appl.* **2026**, *10*, 6.

[7] Huang, T. X.; Cong, X.; Wu, S. S.; Wu, J. B.; Bao, Y. F.; Cao, M. F.; Wu, L. W.; Lin, M. L.; Wang, X.; Tan, P. H. et al. Visualizing the structural evolution of individual active sites in MoS_2 during electrocatalytic hydrogen evolution reaction. *Nat. Catal.* **2024**, *7*, 646–654.

[8] Cai, Q. M.; Gao, R. L.; Wang, Y. F.; Xing, J. S.; Zhang, Q. Y.; Zhu, M. Z.; Qin, X. Y.; Liao, M. H.; Huang, Y. C. Ruthenium containing polyoxometalates: From synthesis, structures, properties to functional applications. *Polyoxometalates* **2025**, *4*, 9140083.

[9] Guo, X. W.; Song, E. H.; Zhao, W.; Xu, S. M.; Zhao, W. L.; Lei, Y. J.; Fang, Y. Q.; Liu, J. J.; Huang, F. Q. Charge self-regulation in 1T‴-MoS_2 structure with rich S vacancies for enhanced hydrogen evolution activity. *Nat. Commun.* **2022**, *13*, 5954.

[10] Chen, L. L.; Huang, Y. C.; Wang, J. J.; Liao, M. H.; Liu, Z. Y.; Liu, M. Q.; Cai, H. Q.; Wang, L.; Gao, L. D.; Hu, D. W. et al. Growth behavior and electronic regulation of Pt on various Mo-based supports for hydrogen evolution electrocatalysis. *Sci. China Chem.* **2025**, *68*,

1837–1846.
[11] Xu, J.; Shao, G. L.; Tang, X.; Lv, F.; Xiang, H. Y.; Jing, C. F.; Liu, S.; Dai, S.; Li, Y. G.; Luo, J. et al. Frenkel-defected monolayer MoS_2 catalysts for efficient hydrogen evolution. *Nat. Commun.* **2022**, *13*, 2193.
[12] Shu, S. Z.; Feng, X.; Sun, J.; Chen, Q. S.; Ou, S. Y.; Zhang, S. X.; Li, Y. H.; Wu, P. F. Polyoxometalates as a precursor in one-pot synthesis of MoS_2–V_2O_5@CC for electrocatalytic hydrogen evolution. *Polyoxometalates* **2026**, *5*, 9140125.
[13] Li, Z. G.; Li, C. L.; Chen, J. W.; Xing, X.; Wang, Y. Q.; Zhang, Y.; Yang, M. S.; Zhang, G. X. Confined synthesis of MoS_2 with rich co-doped edges for enhanced hydrogen evolution performance. *J. Energy Chem.* **2022**, *70*, 18–26.
[14] Hai, G. T.; Xue, X. D.; Wu, Z. Y.; Zhang, C. Y.; Liu, X.; Huang, X. B. High-throughput calculation-based rational design of Fe-doped MoS_2 nanosheets for electrocatalytic pH-universal overall water splitting. *J. Energy Chem.* **2024**, *91*, 194–202.
[15] Li, M. Y.; Cai, B. H.; Tian, R. M.; Yu, X. J.; Breese, M. B. H.; Chu, X. Z.; Han, Z. J.; Li, S.; Joshi, R.; Vinu, A. et al. Vanadium doped 1T MoS_2 nanosheets for highly efficient electrocatalytic hydrogen evolution in both acidic and alkaline solutions. *Chem. Eng. J.* **2021**, *409*, 128158.
[16] Xiong, Y. Z.; Zhao, W.; Chen, C. Z.; Qiu, M. Y.; Dong, Y. R.; Liu, Y. J.; Jiang, J. C.; Fan, M. M.; Wang, K. Activating efficient HMF electro-oxidation activity of biochar-loaded MoS_2 by Co-modified. *Ind. Crops Prod.* **2025**, *224*, 120423.
[17] Li, B. J.; Nie, K. K.; Wang, K. N.; Tang, X. P.; Wang, R. J.; Yi, L. X.; Zhang, Y. J.; Wang, Z. Y.; Wang, J. T.; Hao, X. R. et al. Phase-dependent reverse electronic metal-support interaction to boost alkaline hydrogen evolution. *Adv. Mater.* **2026**, *38*, e18017.
[18] Sun, F. R.; Yang, K. B.; Qin, X. B.; Wu, W. B.; Lu, Y. Z. Achieving highly efficient electrocatalytic hydrogen evolution with Co-doped MoS_2 nanosheets. *Nanoscale Horiz.* **2025**, *10*, 1120–1130.
[19] Li, Z. D.; Yan, X. X.; He, D.; Hu, W. H.; Younan, S.; Ke, Z. J.; Patrick, M.; Xiao, X. H.; Huang, J. E.; Wu, H. J. et al. Manipulating coordination structures of mixed-valence copper single atoms on 1T-MoS_2 for efficient hydrogen evolution. *ACS Catal.* **2022**, *12*, 7687–7695.
[20] Guo, T. X.; Lin, Y. X.; Chen, X.; Lu, J. L.; Zhao, X. L.; Yao, X. J.; Meng, L. J.; Liu, Y. J.; Zhang, X. Y. Metal-nonmetal atom co-doping engineered transition metal disulfide for highly efficient hydrogen evolution reaction. *Int. J. Hydrogen Energy* **2023**, *48*, 2990–2997.
[21] Chen, X.; Sun, J. X.; Guan, J. M.; Ji, J.; Zhou, M.; Meng, L. J.; Chen, M.; Zhou, W. Q.; Liu, Y. J.; Zhang, X. Y. Enhanced hydrogen evolution reaction performance of MoS_2 by dual metal atoms doping. *Int. J. Hydrogen Energy* **2022**, *47*, 23191–23200.
[22] Lu, Y. Z.; Wei, S. Z.; Yang, S. S.; Fu, L. P.; Tang, J. Q.; Liu, Y.; Liu, W. Hydrothermal synthesis and bifunctional electrocatalytic properties of N and Co co-doped MoS_2 for water splitting. *Tungsten* **2025**, *7*, 511–524.
[23] Li, Y. F.; Yuan, X. L.; Wang, P.; Tang, L. L.; He, M.; Li, P. G.; Li, J.; Li, Z. X. Rare earth alloy nanomaterials in electrocatalysis. *J. Energy Chem.* **2023**, *83*, 574–594.
[24] Shen, W.; Zhu, J. M.; Hu, Y.; Yin, J.; Zheng, Y.; Xi, P. X. Applications of rare earth promoted transition metal sulfides in electrocatalysis. *Chin. J. Chem.* **2023**, *41*, 1740–1752.
[25] Peera, S. G.; Kim, S. W. Rare earth Ce/CeO_2 electrocatalysts: Role of high electronic spin state of Ce and Ce^{3+}/Ce^{4+} redox couple on oxygen reduction reaction. *Nanomaterials* **2025**, *15*, 600.
[26] Liu, X.; Liu, T.; Ouyang, T.; Deng, J. G.; Liu, Z. Q. Ce^{3+}/Ce^{4+} ion redox shuttle stabilized $Cu^{\delta+}$ for efficient CO_2 electroreduction to C_2H_4. *Angew. Chem., Int. Ed.* **2025**, *64*, e202419796.
[27] Zhao, H. R.; Yuan, C. Z.; Zhou, C. L.; Zhao, W. K.; Zhang, L. L.; Li, C. H.; Xin, L.; Wu, F. L.; Ye, S. F.; Zhang, X. M. et al. Balancing electron transfer and intermediate adsorption ability of metallic Ni–Fe-RE-P bifunctional catalysts via 4*f*-2*p*-3*d* electron interaction for enhanced water splitting. *J. Energy Chem.* **2024**, *94*, 458–465.
[28] Li, R. Q.; Wang, C. M.; Xie, S. X.; Hang, T. Y.; Wan, X. Y.; Zeng, J. J.; Zhang, W. Coupling MoS_2 nanosheets with CeO_2 for efficient electrocatalytic hydrogen evolution at large current densities. *Chem. Commun.* **2023**, *59*, 11512–11515.
[29] Kong, L. H.; Gao, C.; Liu, Z. X.; Pan, L.; Yin, P. G.; Lin, J. J. Cerium-doped 1 T phase enriched MoS_2 flower-like nanoflakes for boosting hydrogen evolution reaction. *Chem. Eng. J.* **2024**, *479*, 147725.
[30] Chen, T. Y.; Fu, Y. Y.; Liao, W. H.; Zhang, Y. Q.; Qian, M.; Dai, H. J.; Tong, X. F.; Yang, Q. H. Fabrication of cerium-doped CoMoP/MoP@C heterogeneous nanorods with high performance for overall water splitting. *Energy Fuels* **2021**, *35*, 14169–14176.
[31] Xie, L.; Dong, Y. Y.; Ling, H.; Xiang, Z. H.; Wang, J. W.; Zhao, L.; Zhou, X.; He, W. Y.; Zheng, X. J. Balancing hydrogen adsorption/desorption on MoS_2 by Co, V dual-doping for efficient hydrogen evolution reaction. *Appl. Surf. Sci.* **2026**, *720*, 165147.
[32] Jiang, B. L.; Li, J. Y.; Tan, Z. H.; Zhang, K. X.; Jiang, N.; Ma, J. P.; Chen, Y. G. Dual active sites in Ce–Co–Ni heterostructure for efficient hydrogen evolution in alkaline and seawater media. *J. Colloid Interface Sci.* **2025**, *700*, 138400.
[33] Li, X.; Dong, K. X.; Sidra, S.; Kim, D. H.; Tran, D. T.; Kim, N. H.; Lee, J. H. Atomic Pt-promoted hierarchical CoP@CNTs-bridged CeO_2-CoP heterostructure-based hollow microcubes for water electrolysis. *Small* **2025**, *21*, e07407.
[34] Wang, Z. Y.; Chen, X. N.; Ding, Y. R.; Zhu, X. F.; Sun, Z. H.; Zhou, H. T.; Li, X.; Yang, W. X.; Liu, J. L.; He, R. Z. et al. Synthesis of two-dimensional high-entropy transition metal dichalcogenide single crystals. *J. Am. Chem. Soc.* **2025**, *147*, 1392–1398.
[35] Schauer, S.; Beitzinger, B.; Neusser, G.; Kranz, C.; Lindén, M. Precursor inhomogeneities influence the properties of multimetal oxides as shown for $LiNi_{0.5}Mn_{1.5}O_4$ derived from hydrothermally synthesized precursors. *Adv. Sci.* **2025**, *12*, e08174.
[36] Yue, C. L.; Zhou, Y.; Liu, Y.; Feng, C.; Bao, W. J.; Sun, F. Y.; Tuo, Y. X.; Pan, Y.; Liu, Y. Q.; Lu, Y. K. Achieving ultra-dispersed 1T-Co-MoS_2@HMCS via space-confined engineering for highly efficient hydrogen evolution in the universal pH range. *Inorg. Chem. Front.* **2022**, *9*, 2617–2627.
[37] Xiao, B. X.; Pang, H. J.; Yu, X. J.; Hou, Y.; Wu, Q.; Ma, H. Y.; Lai, X. Y.; Wang, X. M.; Tan, L. C.; Yang, G. X. Directly growth of highly uniform MnS–MoS_2 on carbon cloth for advanced H_2 evolution electrocatalyst in different pH electrolytes. *Int. J. Hydrogen Energy* **2022**, *47*, 40872–40880.
[38] Ma, Y. Y.; Lang, Z. L.; Yan, L. K.; Wang, Y. H.; Tan, H. Q.; Feng, K.; Xia, Y. J.; Zhong, J.; Liu, Y.; Kang, Z. H. et al. Highly efficient hydrogen evolution triggered by a multi-interfacial Ni/WC hybrid electrocatalyst. *Energy Environ. Sci.* **2018**, *11*, 2114–2123.
[39] Sanwal, P.; Raza, A.; Miao, Y. X.; Lumbers, B.; Li, G. Advances in coinage metal nanoclusters: From synthesis strategies to electrocatalytic performance. *Polyoxometalates* **2024**, *3*, 9140057.
[40] Bi, H. X.; Guo, M. S.; Du, J.; Ma, Y. Y.; Han, Z. G. Polyoxometalate chemistry of $\{M[P_4Mo_6]_2\}$: From structure assembly to functional application. *Coord. Chem. Rev.* **2024**, *518*, 216092.
[41] Cameron, J. M.; Guillemot, G.; Galambos, T.; Amin, S. S.; Hampson, E.; Mall Haidaraly, K.; Newton, G. N.; Izzet, G. Supramolecular assemblies of organo-functionalised hybrid polyoxometalates: From functional building blocks to hierarchical nanomaterials. *Chem. Soc. Rev.* **2022**, *51*, 293–328.
[42] Cai, H. Q.; Yang, Q. H.; Chen, L. L.; Gao, R. L.; Liao, M. H.; Xing, J. S.; Zhou, W. B.; Pu, N.; Gu, J.; Huang, Y. C. Polyoxometalates-derived Pt–Mo_2C cluster heterostructure for co-catalytic alkaline hydrogen evolution reaction. *Rare Met.* **2025**, *44*, 4701–4711.
[43] Liao, M. H.; Zhu, Q. G.; Li, Y. Y.; Yan, Q. Z.; Zhou, S. S.; Dai, J. J.;

Huang, Y. C.; Gu, J. Polyoxometalates hydrogels derived porous conductive Pt@Mo_2C carbon aerogels as self-supporting electrocatalysts for enhancing alkaline hydrogen evolution reaction. *Rare Met.* **2025**, *44*, 8609–8618.

[44] Xia, K.; Yatabe, T.; Yonesato, K.; Yabe, T.; Kikkawa, S.; Yamazoe, S.; Nakata, A.; Yamaguchi, K.; Suzuki, K. Supported anionic gold nanoparticle catalysts modified using highly negatively charged multivacant polyoxometalates. *Angew. Chem., Int. Ed.* **2022**, *61*, e202205873.

[45] Zeb, Z.; Huang, Y. C.; Chen, L. L.; Zhou, W. B.; Liao, M. H.; Jiang, Y. Y.; Li, H. T.; Wang, L. M.; Wang, L.; Wang, H. et al. Comprehensive overview of polyoxometalates for electrocatalytic hydrogen evolution reaction. *Coord. Chem. Rev.* **2023**, *482*, 215058.

[46] Jia, Y.; Zhang, J.; Zhang, Z. M.; Li, Q. Y.; Wang, E. B. Metal-centered polyoxometalates encapsulated by surfactant resulting in the thermotropic liquid crystal materials. *Inorg. Chem. Commun.* **2014**, *43*, 5–9.

[47] Darii, M.; Beleaev, E. S.; Kravtsov, V. C.; Bourosh, P.; Chumakov, Y.; Hauser, J.; Decurtins, S.; Liu, S. X.; Sultanova, O.; Baca, S. G. Crystalline multicomponent compounds involving hexaammine cobalt(III) cations. *New J. Chem.* **2022**, *46*, 11404–11421.

[48] Bala, R.; Sharma, R. P.; Sharma, U.; Burrows, A. D.; Cassar, K. Hexaamminecobalt(III) complexes as multiple hydrogen bond donors: Synthesis, characterization and X-ray structural study of mixed anion complexes $[Co(NH_3)_6]Br_2(BF_4)$ and $[Co(NH_3)_6]Cl_2(HC_2O_4)\cdot H_2O$. *J. Mol. Struct.* **2007**, *832*, 156–163.

[49] Zeb, Z.; Huang, Y. C.; Chen, L. L.; Gao, R. L.; Gao, X. H.; Sun, M. D.; Cai, H. Q.; Chen, J. C.; Abbas, F.; Liao, M. H. et al. Polyoxometalates metal-organic frameworks-derived transition metal sulfides with rich interfaces for efficient alkaline oxygen evolution reaction. *J. Colloid Interface Sci.* **2025**, *686*, 289–303.

[50] Wang, J. N.; Ling, Q.; Yao, Y. X.; Zhu, D. L.; Shu, S. Z.; Zhou, Z. L.; Wu, X. F.; Wu, P. F. Willow Catkin-Like Co_4S_3–WS_2 nanostructured electrocatalyst for efficient overall alkaline water splitting. *ACS Appl. Nano Mater.* **2024**, *7*, 24408–24416.

[51] Wang, Y. Q.; Wang, T.; Xu, M.; Li, B. W.; Gao, Z.; Zhang, W. J.; Li, Z. X.; Qu, C. Q.; Feng, M. Polyoxometalate superlattices derived bimetallic sulfides to accelerate acidic and alkaline hydrogen evolution reaction. *J. Colloid Interface Sci.* **2025**, *679*, 760–768.

[52] Clark, S. J.; Segall, M. D.; Pickard, C. J.; Hasnip, P. J.; Probert, M. I. J.; Refson, K.; Payne, M. C. First principles methods using CASTEP. *Z. Kristallogr. Cryst. Mater.* **2005**, *220*, 567–570.

[53] Shu, S. Z.; Zhu, D. L.; Wang, X. J.; Sun, J.; Wang, J. N.; Ling, Q.; Zhou, Z. L.; Chen, Y. J.; Wu, P. F. High-performance Co_4S_3–MnS–MoS_2@CC catalysts for the hydrogen evolution reaction. *J. Mater. Chem. A* **2025**, *13*, 17740–17747.

[54] Liu, D. L.; Wang, Z. H.; Zhang, Y.; Zhou, H. Q.; Zhang, Y.; Li, D. Y.; Yu, F. Highly efficient pH-universal hydrogen evolution reaction catalyzed by rapidly reconstructed bimetallic cobalt-molybdenum alloy cuboids arrays. *Nano Res.* **2024**, *17*, 6977–6983.

[55] Petcharat, N.; Kaewmuntree, N.; Krobkrong, N.; Hirunpinyopas, W.; Chavalekvirat, P.; Iamprasertkun, P.; Thanasarnsurapong, T.; Boonchun, A.; Kamonsuangkasem, K.; Sirisaksoontorn, W. The interplay of dy doping and sulfur vacancies in MoS_2 for an efficient hydrogen evolution reaction. *ACS Omega* **2026**, *11*, 16571–16581.

[56] Gurusamy, P.; Perumalsamy, S. V.; Pandian, T.; Vellingiri, G.; Kulanthaivel, J.; Sinthika, S.; Mithra, K. M. Effective solar-driven overall electrocatalytic water-splitting by Co-doped 1T/2H MoS_2 nanoparticles. *Int. J. Hydrogen Energy* **2025**, *130*, 452–461.

[57] Zhang, C. Y.; Yu, J.; Huang, C.; Sun, G. W.; Balcells, L.; Li, J. Y.; Qi, X. D.; Yi, C. Z.; Herrero-Martín, J.; Simonelli, L. et al. Metal doping activation of anion-mediated electron transfer in catalytic reactions. *J. Am. Chem. Soc.* **2025**, *147*, 7070–7082.

[58] Chen, L. L.; Huang, Y. C.; Ding, Y. P.; Yu, P.; Huang, F.; Zhou, W. B.; Wang, L. M.; Jiang, Y. Y.; Li, H. T.; Cai, H. Q. et al. Interfacial engineering of atomic platinum-doped molybdenum carbide quantum dots for high-rate and stable hydrogen evolution reaction in proton exchange membrane water electrolysis. *Nano Res.* **2023**, *16*, 12186–12195.

[59] Deshmukh, M. A.; Bakandritsos, A.; Zbořil, R. Bimetallic single-atom catalysts for water splitting. *Nanomicro Lett.* **2025**, *17*, 1.

[60] Wang, L. X.; Yuan, C. Z.; Li, C. H.; Zhang, Y. R.; Wu, F. L.; Xin, L.; Wang, Z. P.; Yang, H.; Shi, X. X.; Zhang, X. M. et al. Interfacial built-in electric field and interatomic charge transfer synergistically boosting oxygen evolution on CeO_2/Ce–Co_3O_4 electrocatalyst. *Adv. Funct. Mater.* **2025**, *35*, 2502122.

[61] Wang, X. M.; Li, N.; Wang, G. C.; Liu, M.; Zhang, C.; Liu, S. X. Ultrafine nanoclusters unlocked 3d-4f electronic ladders for efficient electrocatalytic water oxidation. *ACS Nano* **2024**, *18*, 20518–20529.

[62] Jung, S. Y.; Kim, D. S.; Rhee, D.; Lee, K. W.; Cho, Y. S.; Alfieri, A. D.; Lynch, J.; Jariwala, D.; Cho, H. K.; Kang, J. Multiscale hierarchically wrinkled MoS_2 nanosheet films with enhanced photoelectrochemical properties. *Chem. Eng. J.* **2026**, *538*, 176992.

[63] Ma, C. H.; Zhu, S. S.; Zhao, Y. C.; Wang, X. Y.; Zhan, T. Z.; Chen, L. H.; Wang, J. N.; Ling, Q.; Xiao, Z. C.; Wu, X. F. et al. CoS_2–MoS_2 nanoflower arrays for efficient hydrogen evolution reaction in the universal pH range. *Langmuir* **2024**, *40*, 744–750.

[64] Wan, C. Z.; Ling, Y. S.; Wang, S. B.; Pu, H. T.; Huang, Y.; Duan, X. F. Unraveling and resolving the inconsistencies in tafel analysis for hydrogen evolution reactions. *ACS Cent. Sci.* **2024**, *10*, 658–665.

[65] Zhang, N.; Li, Y.; Zhang, R. L.; Huang, S. S.; Wang, F.; Tang, M.; Liu, J. Tiny Ni_3S_2 boosting MoS_2 hydrogen evolution in alkali by enlarging coupling boundaries and stimulating basal plane. *J. Colloid Interface Sci.* **2023**, *642*, 479–487.

[66] Das, S.; Banerjee, A.; Nandi, U.; Ghosh, A. Critical review on the analysis of electrochemical impedance spectroscopy data. *J. Appl. Phys.* **2025**, *138*, 125002.

[67] Wang, T.; Chang, P.; Sun, Z. P.; Wang, X. H.; Tao, J. G.; Guan, L. X. Interface prompted highly efficient hydrogen evolution of MoS_2/CoS_2 heterostructures in a wide pH range. *Phys. Chem. Chem. Phys.* **2023**, *25*, 13966–13977.

[68] Chen, L. L.; Huang, Y. C.; Wang, J. J.; Liao, M. H.; Huang, S. X.; Cai, H. Q.; Wang, L.; Zhao, L. M.; Pu, N.; Fan, Z. J. Platinum-dependent 2H-to-1T phases conversion of MoS_2 nanosheets growing on cross-interlocking porous carbon for boosting hydrogen evolution reaction. *Chem. Eng. J.* **2024**, *498*, 155060.

[69] Jin, D. Y.; Qiao, F.; Zhou, Y.; Wang, J. F.; Cao, K. C.; Yang, J.; Zhao, J. K.; Zhou, L.; Li, H. T. Cu/Mo_2C synthesized through Anderson-type polyoxometalates modulate interfacial water structure to achieve hydrogen evolution at high current density. *Nano Res.* **2024**, *17*, 2546–2554.

[70] Tan, X. J.; Wang, Z.; Liu, J. Q.; Yang, J. S.; Wang, Q.; Yuan, S. Synthesis of NiMo–$NiMoO_x$ with crystalline/amorphous heterointerface for enhanced hydrogen evolution reaction. *Nano Res.* **2025**, *18*, 94907368.

[71] Zhu, D. L.; Sun, J.; Shu, S. Z.; Chen, Q. S.; Feng, X.; Zhang, S. X.; Li, Y. H.; Ou, S. Y.; Wu, P. F. Co- and V-doped MoS_2 nanosheet composites for efficient hydrogen evolution reaction in the universal pH range. *Langmuir* **2025**, *41*, 33532–33541.

[72] Chen, L. L.; Huang, Y. C.; Li, H. T.; Gao, R. L.; Tang, H.; Chen, J. W.; Wang, Y. F.; Liao, M. H.; Wu, C. D. Polyoxometalate-derived N@Mo_2C/V_2O_3 cluster heterostructure for accelerated alkaline hydrogen evolution reaction. *Polyoxometalates* **2026**, *5*, 9140110.

[73] Zhu, X.; Chen, L. Y.; Liu, Y. G.; Tang, Z. H. Atomically precise Au nanoclusters for electrochemical hydrogen evolution catalysis: Progress and perspectives. *Polyoxometalates* **2023**, *2*, 9140031.

[74] Lei, T. M.; Wu, S. B.; Zhang, Y. M.; Guo, H.; Chen, D. L.; Zhang, Z. Y. Effects of La, Ce and Nd doping on the electronic structure of

monolayer MoS_2. *Acta Phys. Sin.* **2014**, *63*, 067301.
[75] Liu, Z. Y.; Chen, L. L.; Huang, S. X.; Liu, M. Q.; Ye, Q. M.; Huang, Y. C. A strongly coupled Pt–W_2N heterostructure embedded in porous carbon nanoflowers for seawater electrolysis. *Sci. China Mater.* **2025**, *68*, 3626–3637.
[76] Huang, Y. C.; Shen, H. W.; Wang, L. M.; Xie, H. X.; Liang, D.; Xing, J. S.; Chen, L. L.; Dai, X. D.; Zhou, Y.; Liao, M. H. et al. Achieving ultra-stable hydrogen evolution at 2000 mA cm^{-2} via a hierarchical Pt electrocatalyst with dual charge/mass transfer networks. *Adv. Powder Mater.* **2026**, *5*, 100389.
[77] Lu, J. J. L.; Lau, J. F.; Loh, C. Y.; Putri, L. K.; Kong, X. Y.; Chew, Y. H.; Lee, W. P. C.; Foo, C. Y.; Haw, C. Y.; Yamakata, A. et al. Dual doping-induced gradient charge polarization in a single non-centrosymmetric photocatalyst for efficient hydrogen production and organic oxidation. *Mater. Today Energy* **2025**, *54*, 102085.
[78] Wu, F.; Zhang, X. L.; Wang, L.; Li, G. C.; Huang, J. F.; Song, A. L.; Meng, A. L.; Li, Z. J. Enhanced spin-polarized electric field modulating p-band center on Ni-doped CdS for boosting photocatalytic hydrogen evolution. *Small* **2024**, *20*, 2309439.
[79] Yao, Y. C.; Hu, S. L.; Chen, W. X.; Huang, Z. Q.; Wei, W. C.; Yao, T.; Liu, R. R.; Zang, K. T.; Wang, X. Q.; Wu, G. et al. Engineering the electronic structure of single atom Ru sites via compressive strain boosts acidic water oxidation electrocatalysis. *Nat. Catal.* **2019**, *2*, 304–313.



Pingfan Wu, Distinguished Professor of the inaugural "Nanhu Scholars Program" and Director of the Institute of POMs Materials at Hubei University of Technology. She has presided over and completed multiple national, provincial and ministerial research projects, and published more than 50 SCI papers in top international journals including *Angew. Chem., Int. Ed.*, *Chem. Eng. J.*, and *J. Mater. Chem. A*. A pioneer in engaging undergraduates with no prior research experience in scientific research, she first put forward the innovative philosophy that "Undergraduate research training should commence upon enrollment". Relying on university-level innovation and entrepreneurship projects as an incubation platform, she has successfully implemented an integrated undergraduate-master-doctoral talent training model. She has produced a series of high-quality research achievements with undergraduates as the primary contributors. Her distinctive undergraduate research training system stands out uniquely, with remarkable outcomes in educational innovation, earning wide recognition and acclaim within the domestic academic community.



Xiao Feng is currently a student majoring in Chemical Engineering at Hubei University of Technology. His research focuses on the synthesis and modification of POMs, as well as their applications in catalysis. He is dedicated to exploring the performance and mechanisms of POMs-based materials in green organic synthesis and energy conversion. His research also involves density functional theory (DFT) calculations.



Sizhan Shu is currently a student majoring in Chemical Engineering at Hubei University of Technology, with a research focus on the synthesis and modification of POMs and their applications as precursors in catalysis.



Shuxin Zhang is currently a student majoring in Chemical Engineering at Hubei University of Technology. Her main research direction is the preparation of photocatalysts and electrocatalysts using POMs as precursors.



Yuhan Li is an undergraduate student from the School of Materials and Chemical Engineering, Hubei University of Technology. Her research focus is on the application study of preparing electrocatalysts using POMs as precursors.



Yujiao Huang is currently a student majoring in Chemical Engineering at Hubei University of Technology. Her main research direction is the design and property investigation of polyoxometalate-based functional materials via quantum chemical calculations.

Open Access This article is licensed under the terms of the Creative Commons Attribution 4.0 International License (http://creativecommons.org/licenses/by/4.0/), which permits use, sharing, distribution and reproduction in any medium, provided the original work is properly cited.

© The author(s) 2026. Published by Tsinghua University Press.